Directly Determined Properties of HD 97658 from Interferometric Observations

Tyler G. Ellis[1] , Tabetha Boyajian[1] , Kaspar von Braun[2] , Roxanne Ligi[3] , Denis Mourard[4] , Diana Dragomir[5] ,
Gail H. Schaefer[6] , and Christopher D. Farrington[6]

[1] Louisiana State University 202 Nicholson Hall Baton Rouge, LA 70803; telli17@lsu.edu
[2] Lowell Observatory 1400 W. Mars Hill Road Flagstaff, AZ 86001, USA
[3] INAF-Osservatorio Astronomico di Brera Via E. Bianchi 46 I-23807 Merate, Italy
[4] Université Côte d'Azur, Observatoire de la Côte d'Azur, CNRS, Laboratoire Lagrange, Parc Valrose, F-06108 Nice Cedex, France
[5] Department of Physics and Astronomy, University of New Mexico, 1919 Lomas Blvd NE, Albuquerque, NM 87131, USA
[6] The CHARA Array of Georgia State University, Mount Wilson, CA 91023, USA

Abstract

We conducted interferometric observations with the CHARA Array of transiting super-Earth host HD 97658 and measured its limb-darkened angular diameter to be $\theta_{\mathrm{LD}} = 0.314 \pm 0.004$ mas. The combination of the angular diameter with the Gaia EDR3 parallax value with zero-point correction ($\pi = 46.412 \pm 0.022$ mas, $d = 21.546 \pm 0.011$ pc) yields a physical radius of $R_\star = 0.728 \pm 0.008\ R_\odot$. We also measured the bolometric flux of the star to be $F_{\mathrm{bol}} = 2.42 \pm 0.05 \times 10^{-8}$ erg s^{-1} cm^{-2}, which, together with angular size, allows a measurement of the effective temperature $T_{\mathrm{eff}} = 5212 \pm 43$ K. Our directly determined physical stellar properties are in good agreement with previous estimates derived from spectroscopy. We used our measurements in combination with stellar evolutionary models and properties of the transit of HD 97658 b to determine the mass and age of HD 97658 as well as constrain the properties of the planet. Our results and our analysis of the TESS light curve on the planet (TOI-1821) corroborate previous studies of this system with tighter uncertainties.

1. Introduction

Interferometric observations of stars provide a unique opportunity to directly measure one of the most fundamental parameters of the star: its radius. Interferometry achieves the resolution of an extremely large telescope by combining the light from one or multiple pairs of telescopes across a variety of separations, or baselines. In particular, optical/near-infrared interferometry requires baselines of only tens of meters to achieve resolutions of milliarcseconds (mas). Direct measurements of stellar radii at great precision will in turn reduce uncertainty in other derived stellar parameters (e.g., effective temperature, surface gravity, or density). Direct observations of stellar radii have highlighted a systematic discrepancy between evolutionary models and reality. Boyajian et al. (2012) have shown that stellar evolutionary models underestimate radii by ~5% and overestimate temperatures by ~3% for K and M dwarfs.

Observations with interferometric arrays play an important role in understanding as well as refining exoplanet system properties. In order to understand the properties of the exoplanet, the properties of the star must first be well constrained. In particular, transiting exoplanets provide a measure of the planet's radius, but this measurement is in units of the host star's radius. Any uncertainty or bias in stellar radius will propagate into estimates of the planet's equilibrium temperature, density, habitability, and composition. Interferometry gives a direct measurement of the stellar radius with little or no dependence on stellar models. This technique has been used in the literature to refine the properties of several important systems, such as 55 Cancri, which hosts five radial-velocity exoplanets including another transiting super-Earth (von Braun et al. 2011), and transiting exoplanet host star GJ 436, where evolutionary models underestimated the stellar radius by ~11% (von Braun et al. 2012). There have also been multiple interferometric surveys of large numbers of exoplanet host stars

such as Baines et al. (2008). The field of interferometry has also seen incredible developments in the field of imaging and astrometry with the ESO GRAVITY project (Gravity Collaboration et al. 2017). In 2019, the GRAVITY collaboration announced the first spectrum of an exoplanet observed with interferometry and refined the astrometric position with 100μas precision (Gravity Collaboration et al. 2019).

The exoplanet host star HD 97658 is of particular interest in this regard as it is the home of a transiting super-Earth (Howard et al. 2011; Dragomir et al. 2013). HD 97658 is a bright, $m_V = 7.78$ mag K1 dwarf with a moderately low iron content of [Fe/H] = −0.23 dex, which was discovered to have a Neptunian mass exoplanet by the NASA Eta-Earth Keck-HIRES radial-velocity survey (Howard et al. 2011). Follow-up time series observations with the Spitzer and MOST space telescopes detected a transit whose depth indicated an estimated planetary radius of a few Earth radii (Dragomir et al. 2013; van Grootel et al. 2014). These properties together make HD 97658b a so-called super-Earth (planets with radii of 1–4 $R_\oplus$ and masses of 1–10 $M_\oplus$; Bryan et al. 2019). Super-Earths can take the form of water worlds with a smothering dense atmosphere or rocky behemoths with minimal atmospheres, both often consistent within the uncertainties of planetary mass and radius (Dragomir et al. 2013). Super-Earths captivate planetary scientists as they are the most populous of observed exoplanets (30%–50% of Sun-like stars host one or more super-Earths; Bryan et al. 2019); however, they do not exist within our own solar system and must be studied solely as exoplanets.

We are interested in refining the properties of HD 97658b by directly measuring the host star's properties. In Section 2, we describe the interferometric observations of HD 97658. In Section 3, we report the resulting directly measured angular diameter, bolometric flux. In Section 4, we model and measure the mass of the star. We then derive updated properties of

Table 1
Summary of Observations of HD 97658

Date [UT]	Baseline	Combiner	Brackets	Calibrators
2015-02-04	S1/W1	Classic	5	HD 93152, HD 99267
2015-02-05	S1/W1	Classic	7	HD 95804, HD 99267
2015-02-11	S1/W1	PAVO	4	HD 101688, HD 96738
2017-03-13	W1/W2	VEGA	2	HD 89239
2017-03-17	S2/W2	VEGA	2	HD 107168
2018-04-28	E2/W2	VEGA	2	HD 97638
2019-05-05	S1/W2	VEGA	3	HD 96738
2020-03-05	S2/E2	VEGA	4	HD 96738, HD 107168

Note. Both PAVO and Classic instruments were used in the single baseline mode of the CHARA array, while VEGA uses multiple baselines simultaneously. See ten Brummelaar et al. (2005, their Table 1) for a complete description of the available baselines. Each bracket corresponds to one observation of the target. See Section 2 for further details.

HD 97658 and its planet using the TESS light curve and our measured results. Lastly, in Section 5 we summarize and conclude this work.

2. Interferometric Observations

We observed HD 97658 over the course of several nights using the Georgia State University Center for High Angular Resolution Astronomy (CHARA) Array at the Mount Wilson Observatory using the Classic (near-IR), VEGA (optical), and PAVO (optical) beam combiners (ten Brummelaar et al. 2005; Ireland et al. 2008; Mourard et al. 2009). A summary of the observations is found in Table 1.

An interferometer measures visibilities (V), which quantifies the contrast of the dark and bright parts of the interference fringe pattern. In practice, this is the contrast of the time-averaged minimum and maximum power of the fringe pattern (see Lawson et al. 2000 for a full description of what an interferometer measures, in their Chapter 2.6).

As the visibilities measured at the time of observing include instrumental and atmospheric effects, it is necessary to observe stars with predictable visibilities to calibrate the data. These calibrator stars are observed in sequence with a science star and allow a measure of the combined systematic effects. Calibrators stars are of a known, and ideally unresolved, size.

Each observation consists of bracketed sequences of the form calibrator 1—science target—calibrator 2 (or calibrator 1 again), and then reverse. One bracket is one observation of the target sandwiched by the calibrators.

As the beam combiners used in this work observe in different bandpasses, it is sometimes necessary to use different calibrators for each instrument. Wherever possible, we calibrated the raw square visibilities of the calibrators against each other (von Braun & Boyajian 2017). This provides insight into previously unknown duplicity, activity, or other anomalous behaviors in a calibrator. No stars were expunged from our list of acceptable calibrators for any reason. The limb-darkened angular size of the calibrators and magnitudes are summarized in Table 2.

We chose calibrators for this work using the JMMC Stellar Diameter Catalog (JSDC) version 2 (Chelli et al. 2016; Duvert 2016).[7] Ideally, we restrict our search for calibrators that are

Table 2
Summary of Calibrator Stars Used in all Observing Campaigns

Calibrator	V mag	H mag	θ_{LD} [mas]
HD 89239	6.530	6.599	0.159 ± 0.008
HD 93152	5.285	5.384	0.279 ± 0.012
HD 95804	6.766	6.288	0.208 ± 0.005
HD 96738	5.593	5.442	0.269 ± 0.033
HD 99267	6.606	6.091	0.241 ± 0.006
HD 101688	6.291	5.730	0.281 ± 0.011
HD 107168	6.220	5.969	0.241 ± 0.011

Note. All photometry data are taken from the JMMC Stellar Diameters Catalog v2. The cited angular diameters are limb darkened and estimated using *isoclassify*.

not resolved on the baselines used with beam combiner's bandpass. Unresolved sources have predicted squared visibilities $V^2 \gtrsim 0.9$. Further, we discard potential calibrators that have known duplicity and/or have rapid rotation driving equatorial distention. Lastly, preference is given to calibrators of comparable brightness and with a minimal angular separation in the sky from the science target.

Calibrator selection is a nontrivial process that can affect the uncertainties in final calibrated data. van Belle & van Belle (2005) demonstrated that a 5% uncertainty in the calibrator diameter can propagate up to a $\sigma_{V^2} \sim 0.04$ uncertainty in the calibrated visibilities, though the amount depends on interferometer configuration, instrument, and calibrator size. Oftentimes, for small, faint targets such as HD 97658, most calibrators that are sufficiently small so as to be unresolved are often too faint to be observed. As such, it is sometimes necessary to compromise for partially resolved calibrators. The caveat with such a compromise is that the target's diameter will only be known as well as the calibrators. In this work, the calibrators HD 101688 and HD 96738 are slightly resolved using the PAVO/VEGA beam combiner and S1–W1 baseline, $V^2 \simeq 0.6$. Thus, the predicted angular size of these calibrators are of concern to the error budget. However, within this size regime, $\theta < 0.45$ mas, the dominant source of error is in the measurement of the visibilities rather than assumptions of calibrator size (van Belle & van Belle 2005).

We used the *isoclassify*[8] program to estimate the angular diameters of these calibrators independently of the JMMC's surface brightness relationship method (Huber et al. 2017; Berger et al. 2020). We find the *isoclassify* and JMMC diameters to be consistent, though the adopted *isoclassify* diameters had larger, more conservative uncertainties (an average of 1.9×larger). All of differences in size are less than 1σ, with the average statistical tension $Avg((|\theta_{iso} - \theta_{JMMC}|)/\sqrt{\sigma_{iso}^2 + \sigma_{JMMC}^2}) = 0.33$.

As previously mentioned, the greater uncertainty in the calibrated visibilities from using resolved calibrators is propagated forward into the uncertainty of the fitted angular diameter. We also note that data taken with the VEGA on several nights are calibrated with only a single star. However, our analysis finds consistency in the calibrated results from night to night and between PAVO and VEGA, assuring confidence in our choice of calibrators and calibration methods (Ligi et al. 2016; Baines et al. 2018; Lachaume et al. 2019).

In order to complete an observation, the interferometric fringes must be found by equalizing the optical path length

---

[7] http://www.jmmc.fr/catalog_jsdc.htm

[8] https://github.com/danxhuber/isoclassify

from the stars to the beam combiner through the two telescopes. The fringes are found by scanning the additional path length up and down for one of the telescopes until fringes are detected. In good conditions, scanning initially takes about 5–15 minutes per star and about twice that in difficult observational conditions. Finding the fringe packet for subsequent observations of the same star typically goes much faster, at most a few minutes.

Observations with the Classic beam combiner consist of approximately 2.5 minutes of integration in the H band. Shutter sequences proceed and follow integration. Classic data are reduced using the REDFLUOR package to produce raw squared visibilities, which are then calibrated using the CALIBIR package—both of these software routines are provided as binary executables from CHARA.[9] Classic observes in a single spectral channel at a time and gathers a single data point per bracket.

Observations with the PAVO beam combiner consist of around 2 minutes integration followed by approximately 3 minutes of shutter sequences and dark integration for reduction and calibration. PAVO data are reduced and calibrated using IDL routines, which are also provided by CHARA (Ireland et al. 2008).[10] As PAVO is an integral field unit, it collects a spectra of fringes with each bracket between 630–950 nm bandwidth (resolution $R = 30$; Ireland et al. 2008).

Observations with VEGA require more time. Calibrators are observed during ~15 minutes while the science star is generally observed during ~30 minutes to ensure enough signal. The data are then reduced using the vegadrs pipeline (Mourard et al. 2009, 2011). VEGA's bandpass is broken into 20 nm bins and creates two data points per baseline at a time.

3. Directly Determined Stellar Properties

3.1. Stellar Diameter

The calibrated squared visibilities V^2 can be fit to the radial profile of the 2D Fourier pair of a uniformly illuminated disk or a limb-darkened disk, θ_{UD} and θ_{LD}, respectively. The resulting profile is a function of the projected baseline B, observational wavelength λ, and most importantly the angular size of the object (Hanbury Brown et al. 1974). The functional form, shown in Equation (1) is a combination of Bessel functions of the first kind, $J_\alpha(x)$, scaled with the linear limb-darkening coefficient μ.

$$V^2 = \left[\left(\frac{1-\mu}{2} + \frac{\mu}{3} \right)^{-1} \\ \cdot \left((1-\mu) \cdot \frac{J_1(x)}{x} + \mu\sqrt{\frac{\pi}{2}} \cdot \frac{J_{3/2}(x)}{x^{3/2}} \right) \right]^2 \quad (1)$$

where $x = \frac{\pi B \theta}{\lambda}$.

We fit the uniform disk model, Equation (1) with $\mu = 0$, for the combined data sets using the *Scipy curve_fit* nonlinear least-squares minimization routine (Jones et al. 2001). As part of the fitting process, we find the optimized fit for many realizations of the data set by sampling the wavelength solution uncertainty. The resulting distribution of fits for the uniform disk is $\theta_{UD} = 0.296 \pm 0.004$ mas. We performed the fitting routine for
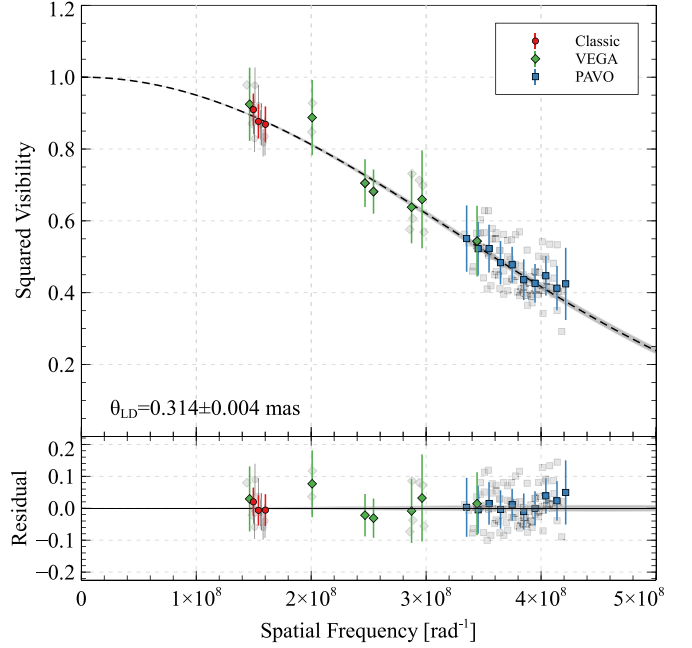
Figure 1. The top panel shows the calibrated squared visibilities and uncertainties from CHARA observations of HD 97658. We binned and averaged the data by equal spacing in of 10^7 rad^{-1} for clarity, and plot these points over all of the calibrated data shown in transparent gray. Classic observations are shown as red circles grouped on the left at lower spatial frequencies, VEGA observations are green diamonds in the middle, and PAVO observations are blue squares grouped on the right at higher spatial frequencies. The fitted visibility curve for a limb darkened disk is shown as a dashed line with the parameters found in Section 3.1. We show the uncertainty in the angular diameter as the gray region around the best-fit curve. The residuals for the fit are shown in the bottom panel. See Section 3.1 for details.

the VEGA and PAVO data sets separately as a check for consistency and found the best-fit uniform disk angular diameters of $\theta_{UD,VEGA} = 0.282 \pm 0.024$ mas and $\theta_{UD,PAVO} = 0.296 \pm 0.004$ mas. As seen in Figure 1, there is more internal spread among the VEGA data than the Classic or PAVO data, which drives the uncertainty up slightly. The enlarged uncertainties are likely caused by dividing the starlight of this faint target among the multiple simultaneous baselines of VEGA. We opt not to perform this same fit with the Classic data as HD 97658 is not well resolved by the instrument, but can still act as a sanity check for the other instruments. The uniform disk angular diameter and other stellar properties are summarized in Table 3.

We fit the limb-darkened disk model using the same technique as above, adding in Monte Carlo realizations of the limb-darkening parameter μ as part of the fitting process. As all visibility curves are near unity at low spatial frequencies, it is safe to combine the Classic data with the VEGA/PAVO data. We estimated the limb-darkening parameter μ using the Limb Darkening Toolkit (LDTK; Husser et al. 2013; Parviainen & Aigrain 2015). Throughout this work we find the limb-darkening coefficient and associated limb darkened diameter in the Bessel R filter. We provide the LDTK module with estimates of T_{eff}, $\log(g) = 4.5 \pm 0.1$, $Z = 0.03 \pm 0.01$. We iterate the fitting process twice to reflect our refined measurements in T_{eff}, which goes into the estimation of the limb-darkening coefficient. The first run uses the fit of θ_{UD} with our measurement of the bolometric flux to estimate T_{eff}, as is discussed in the following section Section 3.2. Then we use the results from the first fit of θ_{LD} to estimate T_{eff} and find our new

Table 3
Summarized Properties of the HD 97658 System

Property	Value	Source
	Measured Stellar Properties	
Parallax [mas]	46.412 ± 0.022	Gaia Collaboration et al. (2021); Lindegren et al. (2021)
Distance [pc]	21.546 ± 0.011	Gaia Collaboration et al. (2021); Lindegren et al. (2021)
[Fe/H] [dex]	-0.23 ± 0.03	Howard et al. (2011)
$\theta_{\mathrm{UD\text{-}R}}$ [mas]	0.296 ± 0.004	Section 3.1 Interferometry
θ_{LD} [mas]	0.314 ± 0.004	Section 3.1 Interferometry
Linear Limb Darkening μ_R	0.629 ± 0.014	Section 3.1 Parviainen & Aigrain (2015); Husser et al. (2013)
$R_\star$ [$R_\odot$]	0.728 ± 0.008	Section 3.1 Interferometry, Parallax
F_{Bol} [erg s^{-1} cm^{-2}]	$2.42 \pm 0.05 \times 10^{-8}$	Section 3.2 SED Templates
T_{eff} [K]	5212 ± 43	Section 3.2 Interferometry, SED
$L_\star$ [$L_\odot$]	0.351 ± 0.007	Section 3.2 F_{Bol}, Parallax
	Isochrone Properties—Section 4.1	
Age [Gyr]	$3.9^{+2.6}_{-2.03}$	Combined Isochrone Models
$M_\star$ [$M_\odot$][a]	$0.773^{+0.015}_{-0.018}$	Combined Isochrone Models
	EXOFASTv2 Model Derived Properties—Section 4.2	
Transit Depth [ppm]	712 ± 38	EXOFASTv2
Period [days]	9.4897116 ± 0.0000008	EXOFASTv2
T_0 [BJD]	2458904.9366 ± 0.0008	EXOFASTv2
$R_p/R_\star$	0.0267 ± 0.0007	EXOFASTv2
Inclination [deg]	$89.05^{+0.41}_{-0.24}$	EXOFASTv2
Impact Parameter	$0.39^{+0.11}_{-0.18}$	EXOFASTv2
Eccentricity	$0.05^{+0.04}_{-0.03}$	EXOFASTv2
$M_\star$ [$M_\odot$][a]	0.75 ± 0.02	EXOFASTv2, MIST
M_p [$M_\oplus$][a]	7.5 ± 0.9	EXOFASTv2, MIST, K
RV Semiamplitude K [m/s]	2.8 ± 0.3	EXOFASTv2, RVs from (Dragomir et al. 2013)
$a/R_\star$	24.2 ± 0.7	EXOFASTv2
R_p [$R_\odot$]	2.12 ± 0.06	Transit Depth, Interferometric $R_\star$
ρ_p [g cm^{-3}]	3.7 ± 0.5	Transit Derived R_p, M_p
T_{Eq} [K]	751 ± 12	EXOFASTv2, $a/R_\star$, T_{eff}
	Stellar and Planetary Properties from Transit Observables—Section 4.3	
$\rho_\star$ [g cm^{-3}]	3.1 ± 0.3	Transit Observed Properties
$M_\star$ [$M_\oplus$][a]	0.85 ± 0.08	Interferometric $R_\star$, Transit Derived $\rho_\star$
log(g) [cgs]	4.64 ± 0.04	Interferometric $R_\star$, Transit Derived $\rho_\star$
Corr($R_\star$, $M_\star$)	0.41	
M_p [$M_\oplus$][a]	8.3 ± 1.1	Transit Derived $M_\star(\rho_\star, R_\star)$ and K
ρ_p [g cm^{-3}]	4.8 ± 0.7	Transit Derived M_p, R_p
Corr(R_p, M_p)	0.09	

Note.
[a] The table reflects the computed mass of the star and planet with two different methods. See Section 4 for more details.

estimation of μ. With the final estimation of μ, we then find our final fit of θ_{LD}. We scale the uncertainties in μ by a factor of 5 during each iteration of the fitting process as the LDTK distribution seems unrealistically tight when compared to Claret & Bloemen (2011), though this does not significantly contribute to the final error budget. Our final estimation of the linear limb-darkening coefficient in the Bessel R filter is $\mu_R = 0.629 \pm 0.014$.

The iteration process resulted in a best-fit limb-darkened angular diameter of $\theta_{\mathrm{LD}} = 0.314 \pm 0.004$ mas. The reduced chi square for the linear limb darkened model is $\chi^2_{\nu=113} = 0.934$ ($p = 0.68$), indicating good agreement between theory and observation. This fit and the calibrated squared visibilities are shown in Figure 1 with the uncertainties scaled to fix χ^2_ν at unity.

We calculate the physical radius of HD 97658 as $0.728 \pm 0.008 \, R_\odot$ using the Gaia EDR3, zero-point corrected parallax measurement (Table 3). Applying the zero-point correction, the Gaia parallax of 46.412 ± 0.022 mas yields a corresponding distance of $d = 21.546 \pm 0.011$ pc (Gaia Collaboration et al. 2021; Lindegren et al. 2021). Previously published radius estimates include Dragomir et al. (2013) who obtained an estimate of $0.703^{+0.035}_{-0.030} \, R_\odot$ from evolutionary models fit within EXOFAST (Eastman et al. 2013) and van Grootel et al. (2014) who derived $0.741^{+0.024}_{-0.023} \, R_\odot$ from the spectroscopic temperature, bolometric correction, and Hipparcos parallax. It is of interest that the estimation of the radius using the evolutionary models in EXOFAST is lower than the spectroscopic radius and the directly measured radius in this paper. As has been explored in Boyajian et al. (2012),

evolutionary models systematically underestimate the radius by a few percent. The high-resolution capabilities of the interferometer complemented with the exquisite parallax measurements from Gaia allow us to report a physical radius with about 1/3 the uncertainty of prior works. The uncertainty in our physical radius predominantly comes from the fit of the angular diameter, with the parallax contribution essentially negligible.

3.2. Bolometric Flux and Temperature

We fit an interpolated K0.5 Pickles (Pickles 1998) template spectrum to collected literature measurements of broadband photometry to measure the bolometric flux. Photometry used in this fit include measurements in Johnson UBV, Cousins R_c, I_C, 2Mass JHK. The photometric measurements are from van Leeuwen (2007), Skrutskie et al. (2006), Kotoneva et al. (2002), Koen et al. (2010), Bessell (2000), Kharchenko (2001), Droege et al. (2006), and Mermilliod (1994).

Interstellar extinction was fixed at 0 in the fitting routine as the proximity of the star should render any extinction effects negligible. The fit was also performed with A_V as a free parameter. This modification found a value of $A_V = 0.027 \pm 0.015$, so we accept our original assumption of no extinction for this work.

The template spectra was then scaled to fit to the photometric measurements and integrated to obtain a bolometric flux $F_{bol} = 2.42 \pm 0.05 \times 10^{-8}$ erg s^{-1} cm^{-2}. We use the updated filter profiles and zero-point corrections as discussed in Mann & von Braun (2015). Further, we account for unknown systematics by applying a 2% addition in quadrature to the bolometric flux uncertainty as is suggested in Bohlin et al. (2014). Our flux measurement and the parallax distance gives a stellar luminosity of $L = 0.351 \pm 0.007 L_\odot$. The assembled photometry and spectral fit are shown in Figure 2. This model has a goodness of fit of $\chi^2_{\nu = 29} = 0.79$ $p = 0.78$. Further details of this technique are available in van Belle et al. (2007) and von Braun & Boyajian (2017). We extended the infrared portion of the spectral energy distribution (SED; $\lambda > 12.5 \mu$m) with the WISE W 1–4 data to check for an infrared excess, but did not observe any such excess (Wright et al. 2010). We note that HD 97658 is saturated in W1 and W2, so we opted to exclude all of these data from the SED fit.

The Stefan–Boltzmann equation can be rewritten to express the temperature in terms of the observables—bolometric flux and angular diameter:

$$T_{eff} = 2341 \cdot \left(\frac{F_{bol}}{\theta^2_{LD}}\right)^{1/4} K, \qquad (2)$$

where the bolometric flux is in units of 10^{-8} erg s^{-1} cm^{-2} and the angular diameter is in mas. We determined an effective temperature of $T_{eff} = 5212 \pm 43$ K given the limb-darkened diameter and above bolometric flux. Howard et al. (2011) measured the effective temperature of HD 97658 as 5170 ± 44 K, which was determined from spectroscopy. This temperature is lower than what we found, but consistent with our result at the 1σ level.

4. Derived Stellar and Planetary Properties

Using the measured properties above, we compute here other properties of the star and its planet. As the host star plays an important role in determining many of the properties of the
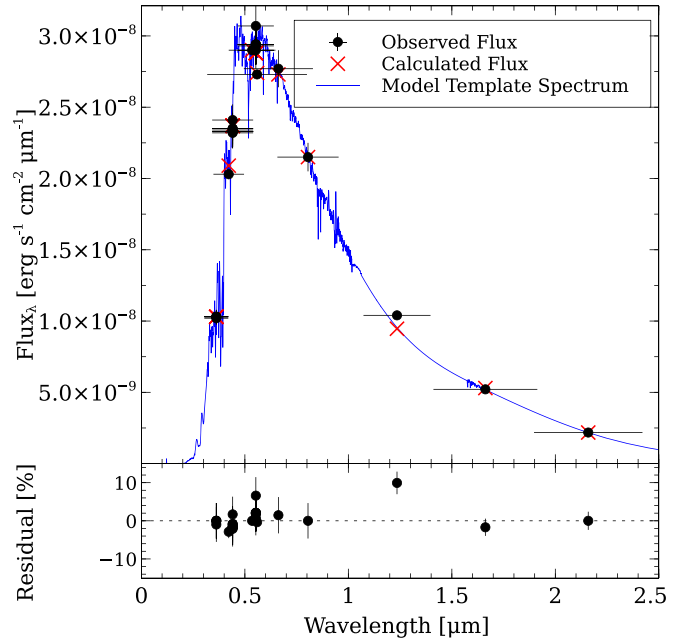
Figure 2. The template spectrum shown in blue is an interpolated Pickles K0.5V stellar spectrum with nominal metallicity. We used literature broadband photometry and associated uncertainties and bandpass widths to scale the spectrum. The photometry is shown as the black points. The horizontal bars on the photometry data points represent the width of the filter bandpass. This scaled spectrum was then integrated to yield the bolometric flux. We calculate the scaled model flux values at the center of the bandpasses and show them as red crosses here. The bottom panel shows the percent residual of this fit. See Section 3.2 for discussion.

planet, we can also update several of the estimated properties of the planet with our improved stellar parameters. We also include new observations of the planet's transit with TESS. A summary of all the following results is shown in Table 3.

4.1. Age and Mass Estimation with Isochrones

We use two stellar evolutionary models to estimate the stellar age and mass. The Garstec and YaPSI stellar evolutionary models (Weiss & Schlattl 2008; Spada et al. 2017) were fit using the bagemass Fortran program (Maxted et al. 2015). These models use our directly measured temperature, the luminosity inferred from the parallax and bolometric flux, the spectroscopically determined [Fe/H] from Howard et al. (2011), and the density inferred from the transit discussed later in this section as predictors of goodness of fit. We assumed uniform priors on age, mass, and surface [Fe/H]. One of the issues with estimating age using isochrones for this range of stellar masses is that a lower mass star afforded a longer time to evolve can have the same observable properties as a higher mass star that is younger. This bias is reflected as the elongated distribution in age and mass. We show the posterior distribution for the YaPSI and Garstec models in Figure 3. We then checked the consistency of the two model's predicted age and mass using a χ^2-test. We first combined (i.e., summed) the two posterior distributions for the ages/masses and computed the resultant median age and mass. We then compute:

$$\chi^2 = \sum_{i=1}^{2} \frac{(x_i - \bar{x})^2}{\sigma^2_i} \qquad (3)$$

where x_i is the median mass/age from the two models, $\bar{x}$ is the median from the combined distribution, and σ is their associated
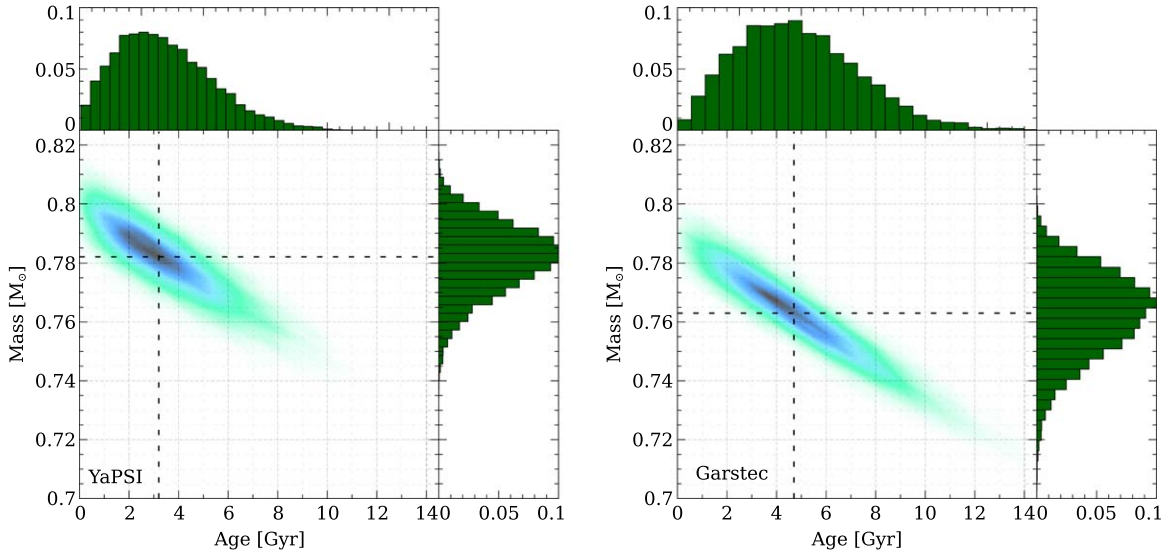
Figure 3. Posterior distribution of age and mass from the *bagemass* Bayesian evolutionary track fitting program as discussed in Section 4. The YaPSI model output is shown on the left and the Garstec model on right. Higher posterior density is shown as the darker regions in the bottom left plot. The posterior population distribution for the ages is shown on the top and the posterior population distribution for the mass is shown on the right. Black dashed vertical/horizontal lines indicate the median for the age $(3.2 \pm 1.9 \text{ Gyr}, 4.7 \pm 2.5 \text{ Gyr})$ and mass $(0.782 \pm 0.011 \, M_\odot, 0.763 \pm 0.011 \, M_\odot)$ for the YaPSI and Garstec models, respectively. We combine the solutions to derive a final estimated age $3.9^{+2.6}_{-2.03}$ Gyr and mass $0.773^{+0.015}_{-0.018} \, M_\odot$ as described in Section 4.
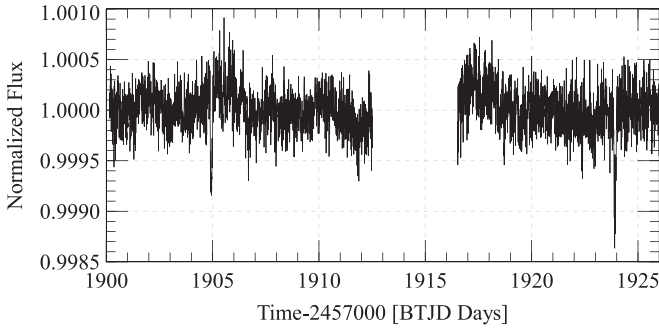
Figure 4. The TESS PSCSAP 2 min light curve binned into 10 minutess bins. The known planet HD 97658b has transits at days 1905 and 1924, as well as a third transit during the gap.

Figure 5. The BLS periodogram of the TESS light curve of HD 97658. The strongest peak coincides with the known planet HD 97658b with a period of ~9.5 days. Most of the other peaks are harmonics of HD 97658b, but there is a notable spike at 1.05 days, which is explored as a potential planet candidate. There is a peak at ~3.8 days, which proved insignificant upon further inspection. The other peaks are harmonics of the 9.5 and 1.05 day signals.

uncertainties. Assuming that these are drawn from a χ^2 distribution, the confidence in the agreement of the two posterior distributions can be computed with:

$$p = \int_{\chi^2}^{\infty} f(\chi^2) d\chi^2. \qquad (4)$$

The χ^2 distribution, $f(\chi^2)$, for this case has $2 - 1 = 1$ degrees of freedom, for the two samples of the age/mass. The computed p value for the ages is $p = 0.62$ and $p = 0.27$ for the masses. Both the mass and age distributions agree within 95% confidence, so we conclude that the median and 1σ confidence interval of the combined distribution is representative of both. The combined isochrone models estimated the age of HD 97658 as $3.9^{+2.6}_{-2.03}$ Gyr and the mass as $0.773^{+0.015}_{-0.018} \, M_\odot$.

HD 97658 has a chromospheric Ca II H and K activity index of $\log(R'_{\text{HK}}) = -4.971$ (Isaacson & Fischer 2010). Isaacson & Fischer (2010) then used the relationship from Mamajek & Hillenbrand (2008, their Equation (3)) to estimate an age of 6.06 ± 0.91 Gyr[11] using the Gaia $G_{\text{BP}} - G_{\text{RP}} = 0.843$ and the

rotation period of 34 ± 2 daysays from Guo et al. (2020), we find another estimate of the age of HD 97658 of 6.25 ± 0.56 Gyr using gyrochronology with stardate (Angus et al. 2019). Both of these techniques agree within ~1σ of the combined isochrone model age from this work.

4.2. Exoplanet Modeling with TESS

The TESS mission (Ricker et al. 2015) observed HD 97658 during Sector 22 for a total duration of approximately 23 days (the full Sector duration of ~27 days, minus ~4 days gap from d13–d17). The normalized PDCSAP light curve is presented in Figure 4. We first use the short cadence (2 minutes) mission processed PDCSAP time series data to look for signs of rotation due to starspots rotating in and out of view on the surface of the star. We find that the average brightness of HD 97658 is stable with a rms (root mean square) of 385 ppm, having no evidence of long-term variability due to spots during this observation period. This conclusion is consistent with TESS observation period being shorter than the derived

---

[11] In order to estimate uncertainty on this age, we applied the suggested rms of 0.07 dex on $\log \tau$ from Mamajek & Hillenbrand (2008).
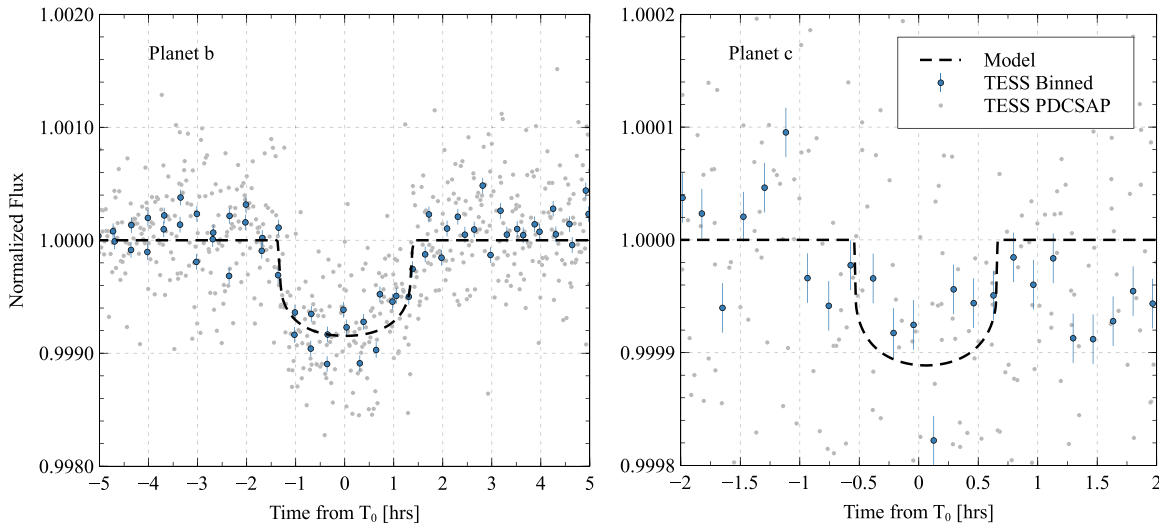
Figure 6. All of the TESS photometry is shown as transparent gray points. The folded and 10 minutess binned TESS photometry with associated errors are shown as blue points. The transit models from EXOFASTv2 are the dashed black line. Left: the best-fit model for planet b with period 9.4896 days. Right: the EXOFASTv2 transit model for the planet candidate "c" identified in Figure 5 with period 1.054 days is shown as the blue dashed line. See Section 4.2 for details. Note that the depth is approximately an order of magnitude less than the left plot.

rotation period $P_{rot} = 34 \pm 2$ days from the spectroscopic analysis of the Calcium H and K lines (S_{HK}; Guo et al. 2020).

Next, we search for transits in the TESS data by computing a box least-squares (BLS) periodogram (Kovács et al. 2002), shown in Figure 5, using the astropy package.[12] We identify the known transiting planet HD 97658 b, with an approximate period of 9.474 days. We note that only two transits of HD 97658b are detected in TESS data, while the third falls within the data gap. We use EXOFASTv2 (Eastman 2017) to simultaneously fit the orbital parameters to the TESS time series along with the full radial-velocity (RV) data series from Dragomir et al. (2013). The program also simultaneously fit the MIST evolutionary models to estimate stellar properties (Choi et al. 2016).

EXOFASTv2 reported a transit depth of HD 97658b of 712 ± 38 ppm with a duration of 2.80 ± 0.04 hr, centered at BJD 2458904.9366 ± 0.0008. With our measurement of the stellar radius and the transit depth, we compute a planet radius of $2.12 \pm 0.06 R_\oplus$. The resultant temperature of HD 97658b can then be found as $T_{eq} = T_\star \sqrt{R_\star / 2a}$, neglecting albedo. We find the equilibrium temperature for planet b of 750 ± 13 K. Our estimation of the equilibrium temperature is in line with the estimate from van Grootel et al. (2014).

Using the planetary mass found with EXOFASTv2, $7.5 \pm 0.9 M_\oplus$, and the planetary radius derived from our direct measurement of the stellar radius and the TESS transit depth, we determine a density of $\rho_p = 3.7 \pm 0.5$ g cm^{-3}. The density is consistent within 1σ of Dragomir et al. (2013) and van Grootel et al. (2014). This fitting of the RV and transit data yielded a semiamplitude of 2.8 ± 0.3 m s^{-1}, which is also within 1σ of Dragomir et al. (2013). The low-amplitude RV signal largely limits the uncertainty in the measurements of planet b's density and any improvements are due to the decreased uncertainty in the transit depth and stellar radius.

Finally, we use the TESS time series to look for any additional transiting planets. Interestingly enough, the BLS periodogram analysis comes up with a signal at 1.054 days. We use EXOFASTv2 to model this candidate signal as an

additional planet in the system at the same time as planet b. If such a planet candidate exists, EXOFASTv2 indicates it would have a period of $1.05443179^{+0.00000011}_{-0.00000018}$ days and cause a transit depth of 88 ± 17 ppm lasting 1.36 hr. The T_0 for the model was found as BJD 2458907.1 ± 0.3. Given this depth and our measurement of the stellar radius, the planet candidate would have a radius of $0.74 R_\oplus$. The planet would be located at 0.019 au with an equilibrium temperature of 1565 K, found using the same method as for planet b. The transit model overlaps with the known planet transit and reduces the depth for planet b to 674 ± 38 and the corresponding radius to $2.06 \pm 0.06 R_\oplus$. The folded light curve for this planet candidate is shown in Figure 6 right panel. The 10 minutes binned out of transit photometry has a root mean square deviation of 39 ppm, about half of the transit depth.

In attempts to verify this signal with existing data, we searched the RV data for a signal with a period of 1.05 daysays, but did not find evidence to support it. However, we note that a transiting planet with this period and transit depth would not be massive enough to induce reflex motions detectable with current RV instruments/observations. We compared the Bayesian information criterion (BIC), a measure of the goodness of the fit that penalizes overparameterization, of the single planet model to the two planet model (Schwarz 1978). We find there is a small preference to the two planet model $\Delta BIC \simeq -8$. However, we still present this signal as only a candidate due to the low strength of the transit signal and lack of RV corroboration.

While beyond the scope of this paper, we propose that further investigation of this candidate would benefit from including archival time series over much longer time baselines than the TESS Sector 22 data presented here. In particular, enabling transit timing variation analysis in the orbital fit for planet b in the model could provide additional independent evidence for the putative companion "c".

4.3. Star and Planet Properties from Transit Observables

Seager & Mallén-Ornelas (2003) demonstrated that combining the transit depth ΔF, duration τ, and period P derived from

---

the exoplanet transit light-curve analysis yield the stellar density. Thus, with a direct determination of the stellar radius through interferometry, we can then directly obtain the stellar mass. This method has been applied to 55 Cnc (Crida et al. 2018b, 2018a) and HD 219134 (Ligi et al. 2019), for which the joint likelihood of the stellar mass and radius ($\mathcal{L}_{MR_\star} = \mathcal{L}_{MR_\star}(\rho_\star, R_\star)$) is expressed through the probability density function (PDF) of the density and radius (see Equation (2) of Ligi et al. 2019). The PDF of the radius is itself expressed as a function of the PDF of the observables θ_{LD} (angular diameter) and d (distance), considered as Gaussian.

This yields the PDF of the planetary mass and radius, which depends on ΔF, P, the semiamplitude of the RV measurement K, and $\mathcal{L}_{MR_\star}$. Importantly, this method also allows computation of the correlation between parameters. This prevents, for example, determining absurd planetary densities that would not correspond to a realistic planetary mass.

Using this technique, and considering only planet b, we obtain $\rho_\star = 3.1 \pm 0.3\,\mathrm{g\,cm^{-3}}$, which yields $M_\star = 0.85 \pm 0.08\,M_\odot$, with a correlation of $\mathrm{Corr}(R_\star, M_\star) = 0.41$. This low correlation is due to the high uncertainty on the stellar density. This direct determination of the mass is higher but consistent with those obtained with the different stellar evolutionary models.

Applying the stellar mass derived from the transit model, the interferometrically derived stellar radius , transit model, and the RV semiamplitude we find the planetary mass $M_p = 8.3 \pm 1.1\,M_\oplus$ and radius $R_p = 2.12 \pm 0.06\,R_\oplus$, with the corresponding density $\rho_p = 4.8 \pm 0.7\,\mathrm{g\,cm^{-3}}$. These measurements are in good agreement with those found from the `EXOFASTv2` analysis. We note that the correlation between the planet's mass and radius is very low ($\mathrm{Corr}(R_p, M_p) = 0.09$). This is explained by $\mathrm{Corr}(R_\star, M_\star)$, which is already low, and the high uncertainty on the transit and RV measurements parameters. Observations with higher precision are needed to reduce these uncertainties and increase the correlation between the parameters.

5. Conclusion

In this work we use the GSU CHARA interferometric array to obtain a highly precise measurement of the angular diameter of HD 97658. We combine measurements from both the infrared Classic instrument as well as the optical PAVO and VEGA instruments for more complete coverage of the UV plane, which helps ensure a well defined angular diameter. We also combine photometric measurements from a panoply of sources to find bolometric flux with SED fitting. These two measurements allow an estimation of temperature independent of distance measurements.

We provide the most direct measurement of the star's radius which paired with the Gaia parallax produce a ∼1% uncertainty in the physical radius and a ∼0.5% uncertainty in effective temperature. Previous works exploring the properties of HD 97658 were able to obtain estimates of the stellar radius and temperatures that are in good agreement with the measurements performed in this work. Because of this we cannot report substantially different composition and properties of HD 97658 b, but we can provide greater certainty in the previous results.

Follow-up observations of HD 97658 with JWST will allow a more precise and accurate measurement of the transit depth. This is a particularly interesting measurement to pin down as current best measurements of the transit depth are accurate to

only ∼5 %, which complicates more accurate analysis of the planet. These follow-up observations would provide further exciting insight into this nearby super-Earth planet. We also eagerly await the Magdalena Ridge Observatory interferometer, which will enable observations of fainter targets and baseline bootstrapping that will ease optimal sampling of the UV plane (Creech-Eakman et al. 2018).

---

[13] Available at http://www.jmmc.fr/catalog_jsdc.htm.
[14] https://www.cosmos.esa.int/gaia
[15] https://archives.esac.esa.int/gaia

Data Availability

The data underlying this article will be shared on reasonable request to the corresponding author. All interferometric data are available in the CHARA archive.[16]

ORCID iDs

Tyler G. Ellis ⓘ https://orcid.org/0000-0001-6584-9919
Tabetha Boyajian ⓘ https://orcid.org/0000-0001-9879-9313
Kaspar von Braun ⓘ https://orcid.org/0000-0002-5823-4630
Roxanne Ligi ⓘ https://orcid.org/0000-0002-6257-6051
Denis Mourard ⓘ https://orcid.org/0000-0001-7425-5055
Diana Dragomir ⓘ https://orcid.org/0000-0003-2313-467X
Gail H. Schaefer ⓘ https://orcid.org/0000-0001-5415-9189
Christopher D. Farrington ⓘ https://orcid.org/0000-0001-9939-2830

References

Angus, R., Morton, T. D., Foreman-Mackey, D., et al. 2019, AJ, 158, 173
Astropy Collaboration, Price-Whelan, A. M., Sipőcz, B. M., et al. 2018, AJ, 156, 123
Baines, E. K., Armstrong, J. T., Schmitt, H. R., et al. 2018, AJ, 155, 30
Baines, E. K., McAlister, H. A., ten Brummelaar, T. A., et al. 2008, ApJ, 680, 728
Berger, T. A., Huber, D., van Saders, J. L., et al. 2020, AJ, 159, 280
Bessell, M. S. 2000, PASP, 112, 961
Bohlin, R. C., Gordon, K. D., & Tremblay, P. E. 2014, PASP, 126, 711
Boyajian, T. S., von Braun, K., van Belle, G., et al. 2012, ApJ, 757, 112
Brasseur, C. E., Phillip, C., Fleming, S. W., Mullally, S. E., & White, R. L. 2019, Astrocut: Tools for creating cutouts of TESS images, Astrophysics Source Code Library, ascl:1905.007
Bryan, M. L., Knutson, H. A., Lee, E. J., et al. 2019, AJ, 157, 52
Chelli, A., Duvert, G., Bourgès, L., et al. 2016, A&A, 589, A112
Choi, J., Dotter, A., Conroy, C., et al. 2016, ApJ, 823, 102
Claret, A., & Bloemen, S. 2011, A&A, 529, A75
Creech-Eakman, M. J., Romero, V. D., Payne, I., et al. 2018, Proc. SPIE, 10701, 1070106
Crida, A., Ligi, R., Dorn, C., Borsa, F., & Lebreton, Y. 2018a, RNAAS, 2, 172
Crida, A., Ligi, R., Dorn, C., & Lebreton, Y. 2018b, ApJ, 860, 122
Dragomir, D., Matthews, J. M., Eastman, J. D., et al. 2013, ApJL, 772, L2
Droege, T. F., Richmond, M. W., Sallman, M. P., & Creager, R. P. 2006, PASP, 118, 1666
Duvert, G. 2016, yCat, II, 345
Eastman, J. 2017, EXOFASTv2: Generalized publication-quality exoplanet modeling code, Astrophysics Source Code Library, ascl:1710.003
Eastman, J., Gaudi, B. S., & Agol, E. 2013, PASP, 125, 83
Foreman-Mackey, D., Agol, E., Angus, R., & Ambikasaran, S. 2017, AJ, 154, 220
Gaia Collaboration, Brown, A. G. A., Vallenari, A., et al. 2021, A&A, 649, A1
Ginsburg, A., Sipőcz, B. M., Brasseur, C. E., et al. 2019, AJ, 157, 98
Gravity Collaboration, Abuter, R., Accardo, M., et al. 2017, A&A, 602, A94
Gravity Collaboration, Lacour, S., Nowak, M., et al. 2019, A&A, 623, L11
Guo, X., Crossfield, I. J. M., Dragomir, D., et al. 2020, AJ, 159, 239
Hanbury Brown, R., Davis, J., Lake, R. J., & Thompson, R. J. 1974, MNRAS, 167, 475
Howard, A. W., Johnson, J. A., Marcy, G. W., et al. 2011, ApJ, 730, 10
Huber, D., Zinn, J., Bojsen-Hansen, M., et al. 2017, ApJ, 844, 102
Husser, T.-O., Wende-von Berg, S., Dreizler, S., et al. 2013, A&A, 553, A6
Ireland, M. J., Mérand, A., ten Brummelaar, T. A., et al. 2008, Proc. SPIE, 7013, 701324
Isaacson, H., & Fischer, D. 2010, ApJ, 725, 875
Jones, E., Oliphant, T., Peterson, P., et al. 2001, SciPy: Open source scientific tools for Python, http://www.scipy.org/
Kharchenko, N. V. 2001, KFNT, 17, 409
Koen, C., Kilkenny, D., van Wyk, F., & Marang, F. 2010, MNRAS, 403, 1949
Kotoneva, E., Flynn, C., Chiappini, C., & Matteucci, F. 2002, MNRAS, 336, 879
Kovács, G., Zucker, S., & Mazeh, T. 2002, A&A, 391, 369
Lachaume, R., Rabus, M., Jordán, A., et al. 2019, MNRAS, 484, 2656
Lawson, P., et al. 2000, Principles of Long Baseline Stellar Interferometry (Pasadena, CA: JPL Publications), 18
Lightkurve Collaboration, Cardoso, J. V. d. M., Hedges, C., et al. 2018, Lightkurve: Kepler and TESS time series analysis in Python, Astrophysics Source Code Library, ascl:1812.013
Ligi, R., Creevey, O., Mourard, D., et al. 2016, A&A, 586, A94
Ligi, R., Dorn, C., Crida, A., et al. 2019, A&A, 631, A92
Lindegren, L., Bastian, U., Biermann, M., et al. 2021, A&A, 649, A4
Mamajek, E. E., & Hillenbrand, L. A. 2008, ApJ, 687, 1264
Mann, A. W., & von Braun, K. 2015, PASP, 127, 102
Maxted, P. F. L., Serenelli, A. M., & Southworth, J. 2015, A&A, 575, A36
Mermilliod, J.-C. 1994, BICDS, 45, 3
Mourard, D., Bério, P., Perraut, K., et al. 2011, A&A, 531, A110
Mourard, D., Clausse, J. M., Marcotto, A., et al. 2009, A&A, 508, 1073
Parviainen, H., & Aigrain, S. 2015, MNRAS, 453, 3821
Pickles, A. J. 1998, PASP, 110, 863
Ricker, G. R., Winn, J. N., Vanderspek, R., et al. 2015, JATIS, 1, 014003
Schwarz, G. 1978, AnSta, 6, 461
Seager, S., & Mallén-Ornelas, G. 2003, ApJ, 585, 1038
Skrutskie, M. F., Cutri, R. M., Stiening, R., et al. 2006, AJ, 131, 1163
Spada, F., Demarque, P., Kim, Y.-C., Boyajian, T. S., & Brewer, J. M. 2017, ApJ, 838, 161
ten Brummelaar, T. A., McAlister, H. A., Ridgway, S. T., et al. 2005, ApJ, 628, 453
van Belle, G. T., Ciardi, D. R., & Boden, A. F. 2007, ApJ, 657, 1058
van Belle, G. T., & van Belle, G. 2005, PASP, 117, 1263
van Grootel, V., Gillon, M., Valencia, D., et al. 2014, ApJ, 786, 2
van Leeuwen, F. 2007, A&A, 474, 653
von Braun, K., & Boyajian, T. 2017, Extrasolar Planets and Their Host Stars (New York: Springer)
von Braun, K., Boyajian, T. S., ten Brummelaar, T. A., et al. 2011, ApJ, 740, 49
von Braun, K., Boyajian, T. S., Kane, S. R., et al. 2012, ApJ, 753, 171
Weiss, A., & Schlattl, H. 2008, Ap&SS, 316, 99
Wright, E. L., Eisenhardt, P. R. M., Mainzer, A. K., et al. 2010, AJ, 140, 1868

[16] http://www.chara.gsu.edu/observers/data-policy-access